FT-IR Transflection Micro-Spectroscopy Study on Normal Human Breast Cells after Exposure to a Proton Beam

Valerio Ricciardi [1,2], Marianna Portaccio [1], Giuseppe Perna [3], Maria Lasalvia [3], Vito Capozzi [3,*], Francesco Paolo Cammarata [4,5], Pietro Pisciotta [5,6,7], Giada Petringa [5], Ines Delfino [8], Lorenzo Manti [2,9] and Maria Lepore [1]

1   Dipartimento di Medicina Sperimentale, Università della Campania "Luigi Vanvitelli", 80138 Napoli, Italy; valerio.ricciardi@unicampania.it (V.R.); marianna.portaccio@unicampania.it (M.P.); maria.lepore@unicampania.it (M.L.)
2   Istituto Nazionale di Fisica Nucleare—Sezione di Napoli, 80100 Napoli, Italy; lorenzo.manti@na.infn.it
3   Dipartimento di Medicina Clinica e Sperimentale, Università di Foggia, 71122 Foggia, Italy; giuseppe.perna@unifg.it (G.P.); maria.lasalvia@unifg.it (M.L.)
4   Istituto di Bioimmagini e Fisiologia Molecolare—Consiglio Nazionale delle Ricerche, 90015 Cefalù, Italy; francesco.cammarata@ibfm.cnr.it
5   Istituto Nazionale di Fisica Nucleare—Laboratori Nazionali del Sud, 95123 Catania, Italy; pietro.pisciotta@lns.infn.it (P.P.); giada.petringa@lns.infn.it (G.P.)
6   Dipartimento di Fisica ed Astronomia "E. Majorana", Università degli Studi di Catania, 95123 Catania, Italy
7   University Medical Center Groningen, Department of Radiotherapy, University of Groningen, 9713 GZ Groningen, The Netherlands
8   Dipartimento di Scienze Ecologiche e Biologiche, Università della Tuscia, 01100 Viterbo, Italy; delfino@unitus.it
9   Dipartimento di Fisica "E. Pancini", Università Degli Studi di Napoli "Federico II", 80126 Napoli, Italy
*   Correspondence: vito.capozzi@unifg.it

Abstract: Fourier transform infrared micro-spectroscopy (μ-FT-IR) is nowadays considered a valuable tool for investigating the changes occurring in human cells after exposure to ionizing radiation. Recently, considerable attention has been devoted to the use of this optical technique in the study of cells exposed to proton beams, that are being increasingly adopted in cancer therapy. Different experimental configurations are used for proton irradiation and subsequent spectra acquisition. To facilitate the use of μ-FT-IR, it may be useful to investigate new experimental approaches capable of speeding up and simplifying the irradiation and measurements phases. Here, we propose the use of low-e-substrates slides for cell culture, allowing the irradiation and spectra acquisition in transflection mode in a fast and direct way. In recent years, there has been a wide debate about the validity of these supports, but many researchers agree that the artifacts due to the presence of the electromagnetic standing wave effects are negligible in many practical cases. We investigated human normal breast cells (MCF-10 cell line) fixed immediately after the irradiation with graded proton radiation doses (0, 0.5, 2, and 4 Gy). The spectra obtained in transflection geometry showed characteristics very similar to those present in the spectra acquired in transmission geometry and confirm the validity of the chosen approach. The analysis of spectra indicates the occurrence of significant changes in DNA and lipids components of cells. Modifications in protein secondary structure are also evidenced.

Keywords: fourier transform infrared micro-spectroscopy; transflection geometry; proton therapy; radiation dose effects; human breast cells

1. Introduction

Fourier transform infrared micro-spectroscopy (μ-FT-IR) has been largely demonstrated to be a valuable tool for investigating the changes occurring in human cells after ionizing radiation exposure. In particular, radiation-induced apoptosis in human lymphocytes was evidenced by Gault and Lefaix [1]. A DNA decreasing content and an increase

in the bands of amide I and II of proteins in the apoptotic cells were inferred from the differences between the spectra from apoptotic and control lymphocytes. These results are in agreement with a possible pathway of radiation-induced apoptosis, which needs active protein synthesis triggered by the occurrence of DNA lesions. μ-FT-IR was demonstrated to be able to investigate the temporal evolution of the apoptosis process [2,3], too. These results concerning early radiation- and oxidative-induced damage to nucleic acids and proteins in single human cells [3] can be evaluated by μ-FT-IR, and are well correlated with established radiobiology techniques. Meade et al. [4] quantitatively analyzed the effects of different γ-radiation doses on the IR spectra of the human keratinocytes cell line (HaCaT). They also investigated the effects at different times after irradiation.

Using μ-FT-IR Gianoncelli et al. [5] explored a different aspect of X-ray induced cellular processes. They investigated the radiation damage of biological samples as a limiting factor when high-resolution X-ray microscopy is performed.

Recently, some of us reported a μ-FT-IR investigation on neuroblastoma cells (SH-SY5Y cell line), in which the use of ratios between absorbances of appropriately chosen peaks was adopted for studying X-ray irradiation effects [6]. This approach represents a very direct way to monitor changes for specific cellular components. Modifications of membrane fluidity and changes in the contributions of the enzymes involved in DNA repair were demonstrated. In addition, the changes for ratio between the absorbance bands of CH_3 and CH_2 asymmetric stretching suggested the occurrence of an apoptotic process also for this cell line. Moreover, the ratios between protein and lipid contents showed significant differences that can be related to changes in membrane characteristics.

In the last ten years, μ-FT-IR has been also applied to the study of biochemical alteration induced in different human cells by particle beams, with particular attention to proton beam irradiation due to the relevance of this treatment in radiotherapy for some cancer types [7,8]. Proton therapy (PT) is not considered currently as the treatment of choice for breast cancer [9]. However, due to the favorable inverted dose-depth profile, which allows greater sparing of normal tissue and organs at risk compared to conventional radiotherapy, the use of PT is clinically justifiable to decrease the risks of radiation-induced cardiovascular disease (CVD) in breast cancer patients [10,11]. Using synchrotron FT-IR spectroscopy, DNA damage and lipid alteration in proton-irradiated cells have been shown [12,13]. These studies were conducted using different methods of sample preparation, irradiation, and spectra acquisition [12–14]. Cells were seeded on ad-hoc Petri dishes with the use of 1.5 μm Mylar foil or 0.5 μm silicon nitride (Si_3N_4) membranes. The latter substrate enabled in-vitro proton irradiation of cells and then spectra acquisition on the same substrate minimizing the number of lost cells treated by radiation [12]. The adopted substrates allow spectra acquisition in transmission geometry but are not easy to handle. The selection of proper substrates represents an important challenge in order to make the μ-FT-IR technique faster and easier to use [15,16]. For this reason, many efforts are underway to identify the most suitable substrate for each type of application [17–19]. MirrIR low-e microscope slides are coated with Ag–SnO_2 and have been generally considered to be good candidates for biological applications. In fact, they are not expensive in comparison with other substrates (like CaF_2, BaF_2, and ZnSe windows), they permit good cell growth and are easy to use. In the present case they can permit proton irradiation and spectra acquisition without any intermediate manipulation. However, there has been considerable debate in the last years about the so-called electric field standing wave (EFCW) effect that can alter FT-IR spectra acquired in a transflection mode questioning their use in biological applications [17,20,21]. Notwithstanding these observations, other researchers [22–25] demonstrated that EFCW effect has a minor role in μ-FT-IR spectroscopy of samples of interest for biological applications. The possibility of using such substrates would allow a faster and easier sample preparation, which is fundamental for possible future use in the clinical setting. For this reason, we propose the use of MirrIR substrates for investigating the effects of proton irradiation on non-cancer human breast cells (MCF-10A) by using μ-FT-IR spectroscopy. This cell line has been selected because the effects of proton irradiation on MCF-10A cells have

been largely examined using clonogenic survival assay, cytokine, chemokine and growth factor analysis, and cDNA micro-array gene expression [26–28]. Since FT-IR results for this cell line are not available, the results of the present investigation have been compared with previous observations obtained with a transmission geometry data collection on different types of cells exposed to proton beams [12–14].

2. Materials and Methods

2.1. Cell Culture

Human normal MCF-10A breast cells (American Type Culture Collection, Manassas, VA, USA) were cultured in DMEM–Ham's F-12 (Sigma–Aldrich, Milano, Italy) supplemented with 100 ng mL^{-1} cholera toxin, 20 ng mL^{-1} epidermal growth factor (EGF), 0.01 mg mL^{-1} insulin, 500 ng mL^{-1} hydrocortisone, and 5% horse serum (Life Technologies, Monza, Italy). Cells were grown in cell culture flasks and cultures were maintained at 37 °C, 5% CO_2. Then, one day before exposure, cells were seeded in polylysine coated MirrIR slides (25 $\times$ 25 mm^2) (Kevley Technologies, Chesterland, OH, USA), a specific reflection FT-IR spectroscopy microscope slide, located inside six well plates, at densities of (5.00 $\pm$ 0.15)·10^4 cells for each well and grown for further 24 h.

2.2. Cell Irradiation and Fixation

Cell irradiation was carried out at the CATANA facility at the Laboratori Nazionali del Sud—Istituto Nazionale di Fisica Nucleare (LNS-INFN) in Catania (Italy), where a 62 MeV proton beam was accelerated by a superconducting cyclotron. In particular, MirrIR slides containing adherent MCF-10A cells derived from one single batch, in order to avoid inter-batch variations, were located in identical flasks, which were placed at the entrance position of a Spread-Out Bragg Peak (SOBP) formed by the optimal stacking of multiple depth dose curves of pristine peaks of different energies using a polymethyl-methacrylate (PMMA) modulator wheel. The SOBP range was about 30 mm in water and the cells were located at a depth of 2.79 mm water equivalent (LET $\approx$ 2.91 keV μm^{-1}). The relative dose profile was measured with a Markus™ ionization chamber (PTW, Freiburg, Germany). A detailed description of beam line and dosimetry is presented elsewhere [29]. Single fractions of 0, 0.5, 2, and 4 Gy were delivered to the plates. A Gafchromic EBT3 film (ISP Corp., New York, NY, USA) was placed on each flask to perform an off-line check about beam flatness and 2D dose distribution. The uncertainty in dose measurements was within 3%. Three MirrIR slides containing the MCF-10A exposed cells were fixed immediately after the end of the exposure process, by means of 3.7% PFA in PBS solution. Samples were subsequently dried at room temperature and kept in a desiccator until analysis to minimize humidity of the samples.

2.3. FT-IR Spectra Measurements

IR absorption spectra of the cell samples were acquired by means of a Spectrum One FT-IR (Perkin Elmer, Shelton, CT, USA) spectrometer equipped with a Perkin Elmer Multiscope system infrared microscope and an MCT (mercury–cadmium–telluride) FPA (focal-plane-array) detector. The measurements were carried out at room temperature on cells grown on MirrIR slides in transflection mode. Three slides were prepared for each experimental condition. Spectra were collected within an aperture of 100 $\times$ 100 μm^2. On each slide, multiple regions were investigated, and three spectra were obtained for each position. The background signal was collected in a region of the slide free of cells. The signal was acquired in the 3600–900 cm^{-1} spectral region using 64 scans with a 4 cm^{-1} spectral resolution and a 5 s acquisition time for each spectrum at room temperature.

2.4. Data Analysis

Preliminary subtraction of the background spectrum acquired in a free-cell zone of the slide was performed for all the spectra. Mie scattering and dispersion artifacts due to scattering between mid-infrared radiation (wavelengths 3–10 μm; ~1000–3000 cm^{-1}) and

cell nuclei and organelles (size between 1–10 μm), were corrected using a Resonant Mie Scattering—Extended Multiplicative Signal Correction (RMieS-EMSC) [30,31]. Afterwards, a piecewise baseline correction was performed, and the spectra were normalized using Standard Normal Variate method [32]. Average spectra with standard deviation were obtained for all sample types. Additionally, second derivative spectra were calculated, using a Savitsky–Golay smoothing algorithm (17 smoothing points) and a 3rd order polynomial approximation, as this approach permits the better resolving of absorption bands [33]. Pre-processing procedures were performed using algorithms written by the authors using MATLAB (ver. 2020, MathWorks Inc., Natick, MA, USA) as interpreter. The spectra were also analyzed by means of convoluted Gauss-cross-Lorentzian shaped vibrational modes. The starting conditions of the procedure were manually selected and a best-fit routine from the GRAMS–AI software (Thermo Fischer Scientific, Waltham, MA, USA) was adopted to evaluate the optimized intensity, position, and width of the peaks. The inflection points were localized in the second-derivative spectra and the χ^2 parameter was employed for assessing the convolution procedure performance. The deconvolution procedure was principally employed for inspecting the changes in the peak position due to proton exposure.

The Amide I band was further analyzed since changes in protein configuration can cause substantial variations in its characteristics [34–36]. To study protein secondary structure, Gauss-cross-Lorentzian shaped components, obtained as before, were used for deconvoluting the Amide I band (1740–1580 cm^{-1}). The area of each absorption band was assumed to be proportional to the relative amount of the structure in infrared spectra [36–38]. Amide III (1350–1200 cm^{-1}) band was also analyzed since it can offer interesting information about secondary protein structures [39] without interference due to residual water content in examined samples.

Further quantitative details on the changes, which are present in the infrared spectra related to different experimental conditions, were acquired by estimating the ratios between the absorbance of selected peaks. The list of the ratios associated to protein content, rearrangement, and phosphorylation, DNA content and modification, lipid content and saturation is shown in Table 1. The ratios values evaluated from the spectra obtained from different samples were compared using a one-way ANOVA test with a 0.05% significance level.

Table 1. A_x/A_y indicate the ratio between the absorbances of selected band [35,40–43]; abbreviation: as = asymmetric, s = symmetric, ν = stretching, δ = bending, sc = scissoring.

Ratio A_X/A_Y	Biomolecular Origin	Indication
A_{1227}/A_{1448}	PO_2^- as. ν /CH_3 as. δ, CH_2 sc.	DNA modification (DNA 1)
A_{1086}/A_{1448}	PO_2^- s. ν /CH_3 as. δ, CH_2 sc.	DNA modification (DNA 2)
A_{1643}/A_{1227}	Amide I/PO_2^- as. ν	Protein/DNA content (PD1)
A_{1643}/A_{1086}	Amide I/PO_2^- s. ν	Protein/DNA content (PD2)
A_{1227}/A_{1086}	PO_2^- as. ν, C-O-P ν/ PO_2^-s. ν, C-O-P ν	DNA modification (DM)
A_{1643}/A_{1534}	Amide I/Amide II	Protein rearrangement (PR1)
A_{1534}/A_{2960}	Amide II/CH_3 as. ν	Protein/Lipid content (PL1)
A_{1394}/A_{2960}	COO− s. ν/CH_3 as. ν	Protein/Lipid content (PL2)
A_{1643}/A_{2960}	Amide I/CH_3 as. ν	Protein/Lipid content (PL3)
A_{2924}/A_{2960}	CH_2 as. ν/CH_3 as. ν	Lipid saturation (LS)
A_{1227}/A_{2960}	PO_2^- as. ν, C-O-P ν/CH_3 as. ν	Protein phosphorylation (PP1)
A_{1086}/A_{2960}	PO_2^- s. ν, C-O-P ν/CH_3 as. ν	Protein phosphorylation (PP2)

3. Results and Discussion

3.1. Analysis of Infrared Spectra from Control and Exposed Cells

In Figure 1, the average FT-IR spectra of control and irradiated cells are reported. As is evident, the experimental approach adopted and the preliminary data treatment

allow to obtain good quality spectra, fully comparable with those collected using different acquisition conditions (see [14]). The spectra here obtained show the presence of several bands related to the vibrational modes of the biologic molecules of cells constituents (lipids, proteins, DNA, etc.). In the panel A and B, the average spectra obtained for the high wavenumber region (HWR) from 3600 to 2600 cm^{-1} and for the fingerprint region (1800–900 cm^{-1}) are, respectively, reported. As expected, the spectra show bands that are due to the contribution of proteins, lipids, and carbohydrates.
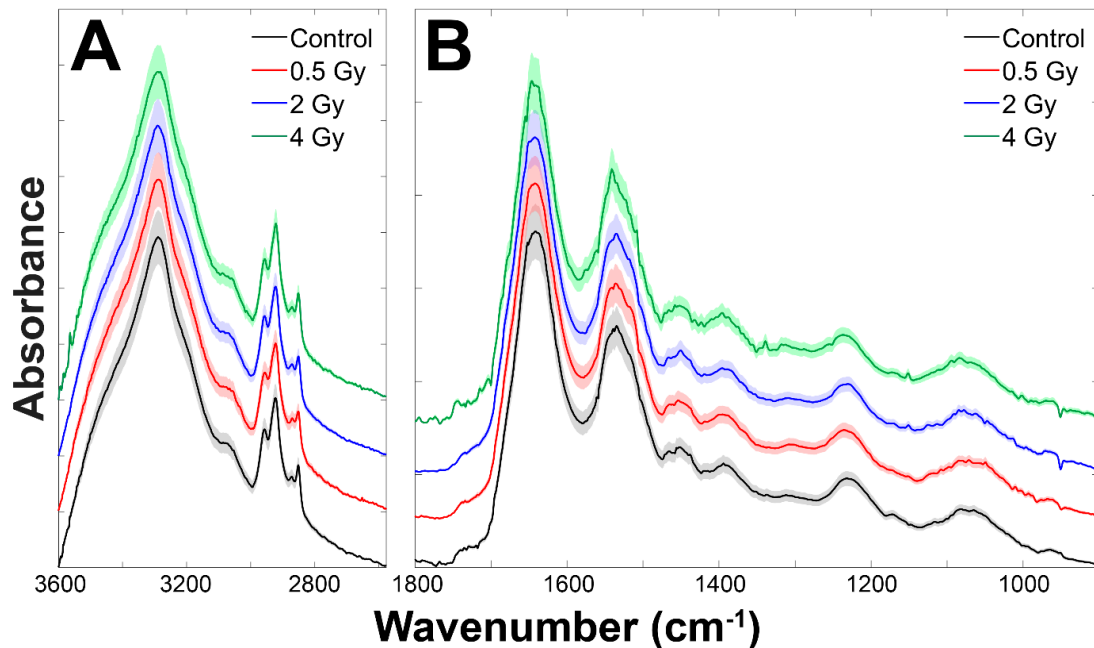

Figure 1. Comparison of average spectra for control and proton irradiated MCF-10A cells (**A**) in the high wavenumber region (3600–2600 cm^{-1}) and (**B**) in the fingerprint region (1800–900 cm^{-1}) at different proton doses (0.5, 2, 4 Gy); data are presented as Mean ± SD. For each dose three slides were examined. On each slide, at least three regions were investigated, and three spectra were obtained for each position. A total number of at least 27 spectra was obtained.

Figure 2A shows the results of deconvolution procedure in the HWR for control samples. In particular, the bands in the range of 3200–3500 cm^{-1} are due to the amide A (–N–H) stretching motion of peptide backbones of proteins amino acids and O–H stretching of carbohydrate polysaccharides, while the band at ≈3170 cm^{-1} is mainly assigned to –NH_3 asymmetric stretching of free amino acids. The two peaks at ≈2960 cm^{-1} and ≈2890 cm^{-1} are related, respectively, to the asymmetric and symmetric stretching of the methyl groups (–CH_3) given by cellular proteins and lipids contribution. The structures at ≈2920 cm^{-1} and ≈2850 cm^{-1} are, respectively, assigned to the asymmetric and symmetric stretching of the methylene groups of membrane lipids (–CH_2).

In Figure 2B, the deconvolution of the fingerprint region for control samples is reported and different peaks that are related to proteins and nucleic acids are evident. The two peaks at ≈1650 cm^{-1} and ≈1540 cm^{-1} are mainly due to the amide I (C=O and C–N) and amide II (N–H and C–N), respectively. The band at ≈1450 cm^{-1} is attributed to symmetric and asymmetric bending of the methylene and methyl groups (–CH_2 and –CH_3) and to –CH_2 scissoring of proteins and lipids, and the feature at 1400 cm^{-1} is due to COO^- group asymmetric stretching of proteins. The asymmetric and symmetric –PO_2^- stretching vibrations of the phosphodiester nucleic acid backbone are associated with the two bands at ≈1230 cm^{-1} and ≈1085 cm^{-1}, respectively, with a contribution from C–O–P stretching of protein and lipids.
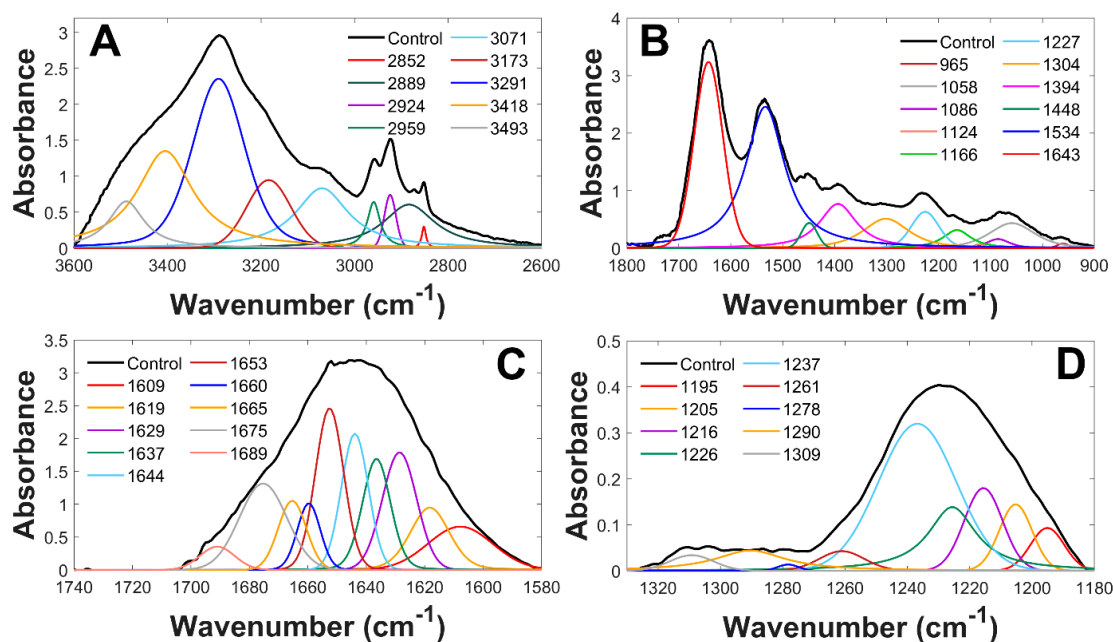
Figure 2. Deconvolution of average control spectra (**A**) in the high wavenumber region (3600–2600 cm^{-1}), (**B**) in the fingerprint region (1800–900 cm^{-1}), (**C**) in the Amide I band region (1740–1580 cm^{-1}) and (**D**) in the Amide III band region (1350–1180 cm^{-1}).

In Table 2, the assignments for all the resolved peaks are shown [2,4–6,35,44]. In addition, the analysis of second derivative spectra (data not shown) of control cells allowed the identification of other contributions. These are also reported in Table 2 in bold characters and they are related to Amide III (1291 cm^{-1}), C-H ring bending (1207 cm^{-1}), sugar -phosphate backbone vibration (1171 cm^{-1}), ribose C-O stretching (1143 cm^{-1}) and P-O-C symmetric stretching (1100 cm^{-1}) [14].

In Table 3, the position of peaks for samples exposed to different doses are reported. The shifts, in terms of wavenumber, of peak positions with respect to those found for the control samples are also reported; shifts higher than the spectral resolution of our experimental apparatus are indicated in bold character.

For the HWR region, the peaks at 2889 and 2852 cm^{-1}, related to membrane lipids and proteins (assigned to CH$_3$ and CH$_2$ symmetric stretching) show a shift beyond spectral resolution, at 0.5 and 2 Gy doses and a shift toward higher wavenumber at 2 and 4 Gy, respectively. It is worthwhile to note that changes in lipid-related peaks are usually associated with membrane fluidity variations [45]. Shifts toward higher wavenumber are also present for the bands at 3173 cm^{-1}, for all the irradiated sample, and for the bands at 3071 for the 0.5 and 2 Gy dose.

In the fingerprint region, significant shifts are observed for 1291 cm^{-1} peak related to Amide III contribution for samples exposed to 0.5 Gy dose and for 1143, 1124, 1058, and 958 cm^{-1} features when samples exposed to the different doses are considered. The latter wavenumber shifts point to changes in DNA conformation [40,46].

Table 2. FT-IR peaks observed in the spectrum of control cells, with assignments in agreement with the data reported in the literature [1,3,4,14,35,47]; abbreviation: as = asymmetric, s = symmetric, ν = stretching, δ = bending, sc = scissoring, vbr = vibration, a. a. = free amino acids. The indicated position of every peak is the centre of the relative Gauss-cross-Lorentzian function obtained from the deconvolution fit. The peaks indicated in bold character are obtained by the analysis of second derivatives.

Peak		Assignment		
cm^{-1}	DNA/RNA	Protein	Lipid	Carbohydrate
3500–3300				O-H ν
3291		Amide A (-N-H ν)		O-H ν

Table 2. *Cont.*

Peak	Assignment			
cm^{-1}	DNA/RNA	Protein	Lipid	Carbohydrate
3173		-NH$_3^+$ as. ν (a. a.)		
3071		Amide B(-N-H ν, δ)		O-H ν
2959		CH$_3$ as. N	CH$_3$ as. ν	
2924			CH$_2$ as. ν	
2889		CH$_3$ s. ν	CH$_3$ s. ν	
2852			CH$_2$ s. ν	
1643		Amide I (C=O ν, C-N ν)		
1534		Amide II (C-Nν,C-NH δ)		
1448		CH$_3$ as. δ, CH$_2$ sc.	CH$_3$ as. δ, CH$_2$ sc.	
1394		COO$^-$ s. ν		
1304		Amide III(-N-Hδ,-C-N ν)		
1291		Amide III(-N-Hδ, -C-N ν)		
1227	PO$_2^-$ as. ν	C-O-P ν		
1207	C-H ring δ			
1171	Sugar -phosphate backbone vbr			
1166			CO-O-C s. as. ν	
1143	Ribose C-O ν			
1124	ν -C-O			
1100	P-O-C s. ν			
1086	PO$_2^-$ s. ν	C-O-P ν		
1058	ν -C-O			
965	PO$_4-$ s. ν	C-0 ν, C=C ν (a. a.)		

Table 3. Average FTIR peaks position for control and samples treated with different doses fixed immediately after irradiation. The shifts in respect of the non-irradiated sample, in terms of units of wavenumber are indicated in brackets (bold values stand for shifts greater than the spectral resolution of the instrument 4 cm^{-1}). Abbreviations: p = proteins, l = lipids, c = carbohydrates.

0 Gy	Assignment	0.5 Gy	2 Gy	4 Gy
Peak (cm^{-1})		Peak (cm^{-1})	Peak (cm^{-1})	Peak (cm^{-1})
3493	c	3490 ($-$3)	3492 ($-$1)	3493
3418	c	3411 ($-$7)	3417 ($-$1)	3421 (+3)
3291	p, c	3291	3291	3295 (+4)
3173	p	3179 (+6)	3178 (+5)	3186 (+13)
3071	p, c	3078 (+7)	3081 (+10)	3071
2959	p, l	2960 (+1)	2960 (+1)	2960 (+1)
2924	l	2924	2924	2923 ($-$1)
2889	p, l	2880 ($-$9)	2880 ($-$9)	2893 (+4)
2852	l	2855 (+3)	2858 (+6)	2859 (+7)
1643	p	1643	1645 (+2)	1644 (+1)
1534	p	1534	1534	1535 (+1)
1448	p, l	1448	1451 (+3)	1451 (+3)
1394	p	1394	1395 (+1)	1396 (+2)

Table 3. *Cont.*

0 Gy	Assignment	0.5 Gy	2 Gy	4 Gy
1304	p, l	1304	1303 (−1)	1311 (+7)
1291	p	1286 (−5)	1295 (+4)	1287 (−4)
1227	DNA, c	1227	1231 (+4)	1233 (+5)
1207	DNA, RNA	1203 (−4)		1202 (−5)
1171	DNA	1171	1171	1169 (−2)
1166	l	1166	1170 (+4)	1167 (+1)
1143	DNA	1149 (+5)		
1124	DNA	1124	1121 (−3)	1116 (−8)
1100	DNA	1098 (−2)		1097 (−3)
1086	DNA, p	1086	1085 (−1)	1084 (−2)
1058	DNA, p	1058	1051 (−7)	1058
958	DNA, p	965 (+7)		966 (+8)

3.2. Analysis of Amide I and Amide III Bands

The analysis of the different peaks constituting the Amide I band can give accurate information on the secondary structure of proteins and their conformational changes due to different doses of ionizing radiation [6,36–38]. The Amide I band (Figure 2C) can be considered as a convolution of the contributions due to the various secondary structures of proteins; the bands between 1620–1640 cm^{-1} and ≈1690 cm^{-1} can likely be attributed to β-sheet structures with the ≈1620 and 1690 cm^{-1} band characteristic of the anti-parallel β-sheet structures. The band at ≈1660 cm^{-1} is principally assigned to α-helix secondary structures, while the random structures and β-turns make a contribution to the bands at ≈1650 and in the 1670–1685 cm^{-1} range, respectively. In the present case, the analysis of the Amide I band of control samples and irradiated samples was performed using ten subcomponents related to parallel β-sheet (1629, 1637 cm^{-1}), anti-parallel β-sheet (1609, 1619 cm^{-1}), α-helix (1653, 1660 cm^{-1}), and β-turn (1665, 1675, 1689 cm^{-1}); unordered structures are attributed to the band at 1644 cm^{-1}.

In the present case, the ratios between the area of the different subcomponents of the Amide I band and the area of the entire Amide I band do not show statistically significant variations when the different proton doses are considered (data not shown). Since Amide I band analysis did not evidence any variation in the secondary structure of cell protein content, the deconvolution of Amide III region (Figure 2D) was performed in order to obtain additional information. In fact, also the Amide III region can offer interesting information about secondary protein structure [39]. The spectral band in 1290–1330 cm^{-1} range is generally assigned to the α-helix secondary structure. Assignments for random coil (1240–1270 cm^{-1}) and β-sheets (1180–1240 cm^{-1}) were also determined [39,48]. In Figure 3, it is evident that the largest contribution to the Amide III band is due to the β-sheets component that does not show any significant changes for the different doses here investigated. Conversely, the α-helix component shows a significant increase for the 2 and 4 Gy doses. The random coil contribution shows a large change for 0.5 Gy dose. Using Amide III band deconvolution changes in the protein secondary structure induced by proton irradiation has been noted. In Table 4 detailed information on the different subcomponent contributions to Amide III is reported. The Amide changes here discussed for proton irradiated cells had not so far been shown using μ-FT-IR [12–14].
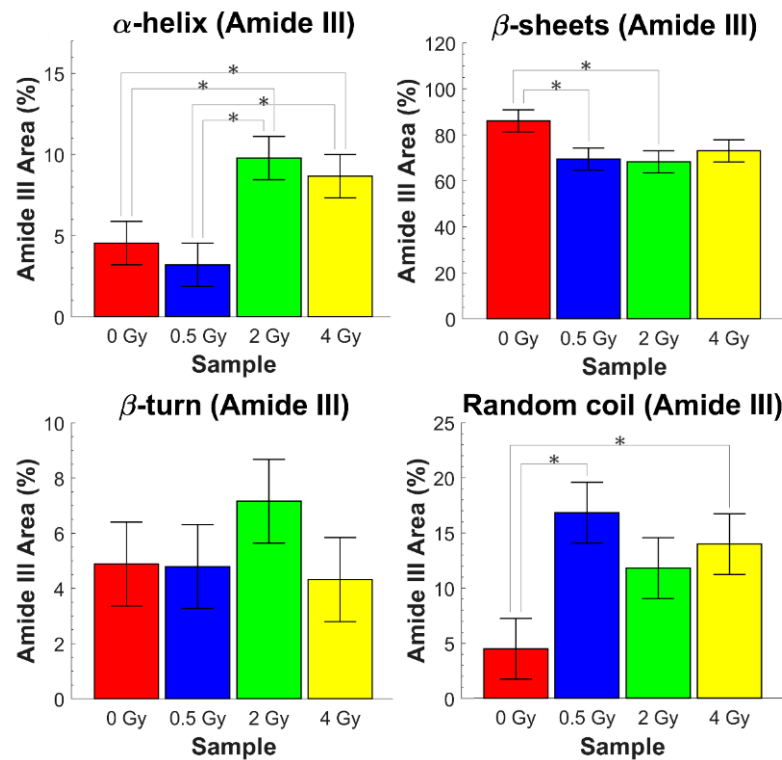
Figure 3. Variations of secondary protein structure contributions to Amide III band (1350–1180 cm^{-1}) with dose, for cells fixed immediately after irradiation; the ratios between the secondary structure peak areas and the area of the entire Amide III peak are reported as Mean ± SD. Asterisks indicate when a significant difference with respect to the corresponding control value occurred at $p \leq 0.05$.

Table 4. Amide III deconvolution results for control and irradiated sample fixed immediately after irradiation, with assignments in accordance with the data reported in the literature [39,48]. The ratios between the area of the different subcomponents and the area of the entire Amide III band are reported as a mean value of percentage (A%) ± SD.

		t_0 Cells		
Control	**Assignments**	**0.5 Gy**	**2 Gy**	**4 Gy**
Peak (cm^{-1})				
1180–1240 %A = 86 ± 8	β-sheets	- %A = 74 ± 15	- %A = 74 ± 20	- %A = 76 ± 15
1240–1270 %A = 4 ± 2	Random coil	- %A = 23 ± 7	- %A = 22 ± 7	- %A = 16 ± 7
1270–1290 %A = 5 ± 2	β-turn	- %A = 7 ± 3	- %A = 7 ± 5	- %A = 7 ± 3
1290–1330 %A = 5 ± 2	α-helix	- %A = 10 ± 4	- %A = 10 ± 4	- %A = 13 ± 5

3.3. Analysis of Relative Absorbance Ratios

The intensity of an infrared band is considered to be proportional to the concentration of the species that are associated with the band. However, the use of band absorbance values, themselves for quantitative analysis, can be influenced by experimental artifacts such as variations in sample thickness. For this reason, it is preferable to use their ratios [41,49,50]. In Table 1, the ratios between the absorbance of chosen bands used in this work are listed, the biochemical processes to which they are related are also indicated.

In the panels of Figure 4, the values of the different ratios mentioned in Table 1 are

reported as a function of the dose. As is evident, only some of these ratios show statistically significant variations. Some of the ratios related to DNA modifications (DNA1 and DM) are among these. DNA1, DNA2, and DM indicate changes in the antisymmetric and symmetric O-P-O stretching modes that are related to double-strand breaks (DBS) [12,42]. DNA1 and DNA2 show an increase when proton dose increases, while DM shows a decrease when proton dose raises. The modifications evidenced by DNA1, DNA2, and DM are in agreement with the results obtained in other cell systems exposed to ionizing radiation that indicate the occurrence of damage in the primary, secondary, and tertiary structure of nucleic acid [42].
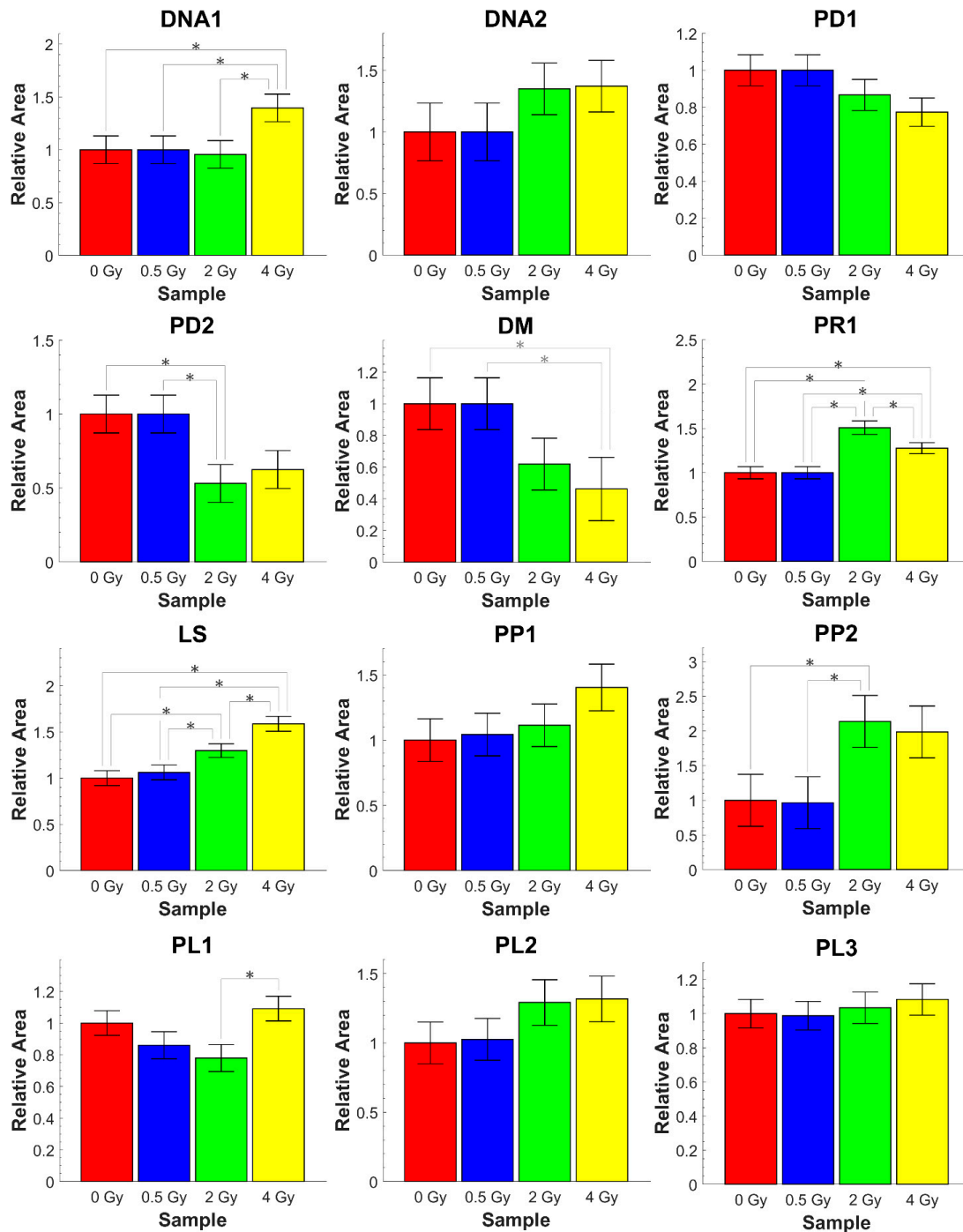
Figure 4. Comparison of the absorbance area ratios for different proton doses. See Table 1 for details on the reported ratios (Mean ± SD) that are normalized to the corresponding ratio value the non-irradiated sample. Asterisks indicate when a significant difference occurred at *p* < 0.05.

The LS ratio gives an indication about lipid saturation and shows a statistically significant increasing trend with proton dose in agreement with results obtained when human cells are exposed to X-ray doses [6,47]. These modifications are suggestive of apoptosis, for which several membrane changes, such as phosphatidylserine exposure, membrane blebbing, and vesicle formation, are known to represent early events [51]. In addition, an increase in saturated fatty acids containing phospholipids during apoptosis in neuronal cells was reported in [40]. Phospholipids are the most relevant structural components of membranes bounding many intracellular organelles (e.g., lysosomes, endoplasmic reticulum, and nuclei) and a relevant change in their composition could induce deformation and porosity of such membranes. Therefore, a characteristic cleavage and laddering of chromosomal DNA occur caused by a deoxyribonuclease flow entering the nucleus during apoptosis process. Singh et al. [52] also indicated that an increase by 10–20% in saturated fatty acids in a mixed population of apoptotic and non-apoptotic cells can be due to the occurrence of a significant increase in saturated fatty acids only in the apoptotic cells. The possible occurrence of apoptosis is also in agreement with the results of a Raman micro-spectroscopy investigation already reported ([6,43,53], and references therein).

The ratios PP1 and PP2, which are both linked to protein phosphorylation [54], show an increasing trend with dose, but only PP2 variations are statistically significant. These modifications indicate the occurrence of changes in the DNA conformation, from the B–DNA form to the A–DNA form already noticed in [6,42,43].

The ratios PL1, PL2, and PL3 are linked to cell protein and lipid content. In particular, the presence of PL1 and PL2 changes would indicates modifications in membrane fluidity and their protein content [6,36]. In the present case, a significant change is noticed only for PL1 when samples exposed to 2 and 4 Gy are considered.

4. Conclusions

Our results concerning MCF-10A cells fixed immediately after the end of the exposure to radiation suggest that the use of MirrIR substrate can offer a fast, reliable, and less expensive experimental approach for proton irradiation and μ-FT-IR investigation, considering the greater ease of handling of samples during preparation and irradiation phase (e.g., low risk of breakage compared to thin mylar sheets). This can be particularly useful when μ-FT-IR spectroscopy is performed for investigating large area samples in which many cells are positioned, as in the present case. The spectra obtained for normal human breast cells exposed to different doses of protons and fixed immediately after the irradiation show spectral characteristics similar to those obtained with other experimental approaches previously mentioned [12–14].

The spectra analysis performed by using deconvolution procedures and the evaluation of the ratio between the area of selected peaks allowed us to prove changes in the DNA and lipid regions, in agreement with the results previously reported [12,14,42]. The Amide I and Amide III regions were also studied and the occurrence of faint changes in protein secondary structure due to proton irradiation have been evidenced for the first time to our knowledge.

The results here reported can be considered as a starting point to evaluate the use of the proposed approach for FT-IR spectroscopy in the field of cells radiobiological response. However, other steps are needed before such a technique is established as a predictor of cellular radio response. In fact, our results pertain to cells fixed immediately after radiation exposure, but it is known that for several hours after irradiation cells try to repair radiation-induced DNA damage. Therefore, future measurements should be performed using cells fixed at different times after exposure, in order to evaluate the evolution over time of the biochemical alterations produced by proton irradiation and possibly compare them with those elicited by photon irradiation as used in conventional radiotherapy.

References

1. Gault, N.; Lefaix, J.L. Infrared microspectroscopic characteristics of radiation-induced apoptosis in human lymphocytes. *Radiat. Res.* **2003**, *160*, 238–250. [PubMed]
2. Gasparri, F.; Muzio, M. Monitoring of apoptosis of HL60 cells by Fourier-transform infrared spectroscopy. *Biochem. J.* **2003**, *369*, 239–248. [PubMed]
3. Gault, N.; Rigaud, O.; Poncy, J.L.; Lefaix, J.L. Infrared microspectroscopy study of γ-irradiated and H_2O_2-treated human cells. *Int. J. Radiat. Biol.* **2005**, *81*, 767–779. [PubMed]
4. Meade, A.; Clarke, C.; Byrne, H.; Lyng, F. Fourier transform infrared microspectroscopy and multivariate methods for radiobiological dosimetry. *Radiat. Res.* **2010**, *173*, 225–237. [PubMed]
5. Gianoncelli, A.; Vaccari, L.; Kourousias, G.; Cassese, D.; Bedolla, D.E.; Kenig, S.; Storici, P.; Lazzarino, M.; Kiskinova, M. Soft X-ray microscopy radiation damage on fixed cells investigated with synchrotron radiation FT-IR microscopy. *Sci. Rep.* **2015**, *5*, 10250.
6. Ricciardi, V.; Portaccio, M.; Manti, L.; Lepore, M. An FT-IR microspectroscopy ratiometric approach for monitoring X-ray irradiation effects on SH-SY5Y human neuroblastoma cells. *Appl. Sci.* **2020**, *10*, 2974. [CrossRef]
7. Paganetti, H. *Proton Therapy Physics*; CRC Press, Taylor and Francis Group: Boca Raton, FL, USA, 2012.
8. Goitein, M. *Radiation Oncology: A Physicist's Eye View*; Springer: New York, NY, USA, 2007.
9. Chowdhary, M.; Lee, A.; Gao, S.; Wang, D.; Barry, P.N.; Diaz, R.; Bagadiya, N.R.; Park, H.S.; Yu, J.B.; Wilson, L.D.; et al. Is Proton Therapy a "Pro" for Breast Cancer? A Comparison of Proton vs. Non-proton Radiotherapy Using the National Cancer Database. *Front. Oncol.* **2018**, *8*, 678.
10. Cheng, Y.J.; Nie, X.Y.; Ji, C.C.; Lin, X.X.; Liu, L.J.; Chen, X.M.; Yao, N.; Wu, S.H. Long term cardiovascular risk after radiotherapy in women with breast cancer. *J. Am. Heart Assoc.* **2017**, *6*. [CrossRef]
11. Jimenez, R.B.; Hickey, S.; DePauw, N.; Yeap, B.Y.; Batin, E.; Gadd, M.A.; Specht, M.; Isakoff, S.J.; Smith, B.L.; Liao, R.C.; et al. Phase II study of proton beam radiation therapy for patients with breast cancer requiring regional nodal irradiation. *J. Clin. Oncol.* **2019**, *37*, 2778–2785.
12. Lipiec, E.; Birarda, G.; Kowalska, J.; Lekki, J.; Vaccari, L.; Wiecheć, A.; Wood, B.R.; Kwiatek, W.M. A new approach to studying the effects of ionising radiation on single cells using FT-IR synchrotron microspectroscopy. *Radiat. Phys. Chem.* **2013**, *93*, 135–141.
13. Lipiec, E.; Bambery, K.R.; Heraud, P.; Hirschmugl, C.; Lekki, J.; Kwiatek, W.M.; Tobin, M.J.; Vogel, C.; Whelan, D.; Wood, B.R. Synchrotron FT-IR shows evidence of DNA damage and lipid accumulation in prostate adenocarcinoma PC-3 cells following proton irradiation. *J. Mol. Struct.* **2014**, *1073*, 134–141. [CrossRef]
14. Lipiec, E.; Kowalska, J.; Lekki, J.; Wiechec, A.; Kwiatek, W.M. FT-IR Microspectroscopy in Studies of DNA Damage Induced by Proton Microbeam in Single PC-3 Cells. *Acta Phys. Pol. A* **2012**, *121*, 506–509. [CrossRef]
15. Baker, M.J.; Trevisan, J.; Bassan, P.; Bhargava, R.; Butler, H.J.; Dorling, K.M.; Fielden, P.R.; Fogarty, S.W.; Fullwood, N.J.; Heys, K.A.; et al. Using Fourier transform IR spectroscopy to analyze biological material. *Nat. Protoc.* **2014**, *9*, 1771–1791. [CrossRef]
16. Perna, G.; Capozzi, V.; Lasalvia, M. A comparison between FTIR spectra from HUKE and SH-SY5Y cell lines grown on different substrates. *Appl. Sci.* **2020**, *10*, 8825. [CrossRef]
17. DeVetter, B.M.; Kenkel, S.; Mittal, S.; Bhargava, R.; Wrobel, T.P. Characterization of the structure of low-e-substrate and consequence for IR transflection measurements. *Vib. Spectrosc.* **2017**, *91*, 119–127. [CrossRef]
18. Rutter, A.V.; Crees, J.; Wright, H.; Raseta, M.; van Pittius, D.G.; Roach, P.; Sulé-Suso, J. Identification of a glass substrate to study cells using Fourier Transform Infrared spectroscopy: Are we close to a spectral pathology? *Appl. Spectrosc.* **2020**, *74*, 178–186. [CrossRef]

19. Yao, J.; Li, Q.; Zhou, B.; Wang, D.; Wu, R. Advantages of infrared transflection micro spectroscopy and paraffin-embedded sample preparation for biological studies. *Spectrochim. Acta Part A Mol. Biomol. Spectrosc.* **2018**, *195*, 25–30. [CrossRef]

20. Filik, J.; Frogley, M.D.; Pijanka, J.K.; Wehbe, K.; Cinque, G. Electric field standing wave artefacts in FT-IR micro-spectroscopy of biological materials. *Analyst* **2012**, *137*, 853–861. [CrossRef]

21. Staniszewska-Slezak, E.; Rygula, A.; Malek, K.; Baranska, M. Transmission versus transflection mode in FT-IR analysis of blood plasma: Is the electric field standing wave effect the only reason for observed spectral distortions? *Analyst* **2015**, *140*, 2412–2421. [CrossRef]

22. Wrobel, T.P.; Wajnchold, B.; Byrne, H.J.; Baranska, M. Corrigendum. Electric field standing wave effects in FT-IR transflection spectra of biological tissue sections: Simulated models of experimental variability. *Vib. Spectrosc.* **2014**, *71*, 115–117. [CrossRef]

23. Cao, J.; Ng, E.S.; McNaughton, D.; Stanley, E.G.; Elefanty, A.G.; Tobin, M.J.; Heraud, P. Fourier transform infrared microspectroscopy reveals that tissue culture conditions affect the macromolecular phenotype of human embryonic stem cells. *Analyst* **2013**, *138*, 4147–4160. [CrossRef]

24. Perez-Guaita, D.; Heraud, P.; Marzec, K.M.; De La Guardia, M.; Kiupel, M.; Wood, B.R. Comparison of transflection and transmission FT-IR imaging measurements performed on differentially fixed tissue sections. *Analyst* **2015**, *140*, 2376–2382. [CrossRef]

25. Lee, J. On the non-existence of the so-called "electric field standing wave effect in transflection FTIR spectra. *Vib. Spectrosc.* **2017**, *90*, 104–111. [CrossRef]

26. Kim, B.; Bae, H.; Lee, H.; Lee, S.; Park, J.C.; Kim, K.R.; Kim, S.J. Proton Beams Inhibit Proliferation of Breast Cancer Cells by Altering DNA Methylation Status. *J. Cancer* **2016**, *7*, 344–352. [CrossRef]

27. Bravatà, V.; Minafra, L.; Cammarata, F.P.; Pisciotta, P.; Lamia, D.; Marchese, V.; Petringa, G.; Manti, L.; Cirrone, G.A.P.; Gilardi, M.C.; et al. Gene expression profiling of breast cancer cell lines treated with proton and electron radiations. *Br. J. Radiol.* **2018**, *91*, 20170934. [CrossRef]

28. Bravatà, V.; Cammarata, F.P.; Minafra, L.; Pisciotta, P.; Scazzone, C.; Manti, L.; Savoca, G.; Petringa, G.; Cirrone, G.A.P.; Cuttone, G.; et al. Proton-irradiated breast cells: Molecular points of view. *J. Radiat. Res.* **2019**, *60*, 451–465. [CrossRef]

29. Cirrone, G.A.P.; Cuttone, G.; Lojacono, P.A.; Lo Nigro, S.; Mongelli, V.; Patti, I.V.; Privitera, G.; Raffaele, L.; Rifuggiato, D.; Sabini, M.G.; et al. A 62-MeV proton beam for the treatment of ocular melanoma at Laboratori Nazionali del Sud-INFN. *IEEE Trans. Nucl. Sci.* **2004**, *51*, 3568–3662. [CrossRef]

30. Bassan, P.; Byrne, H.J.; Bonnier, F.; Lee, J.; Dumas, P.; Gardner, P. Resonant Mie scattering in infrared spectroscopy of biological materials–understanding the 'dispersion artefact'. *Analyst* **2009**, *134*, 1586–1593. [CrossRef]

31. Bassan, P.; Kohler, A.; Martens, H.; Lee, J.; Byrne, H.J.; Dumas, P.; Gazi, E.; Brown, M.; Clarke, N.; Gardner, P. Resonant Mie scattering (RMieS) correction of infrared spectra from highly scattering biological samples. *Analyst* **2010**, *135*, 268–277. [CrossRef]

32. Lasch, P. Spectral pre-processing for biomedical vibrational spectroscopy and microspectroscopic imaging. *Chem. Intell. Lab. Syst.* **2012**, *117*, 100–114. [CrossRef]

33. Lipiec, E.; Bambery, K.R.; Lekki, J.; Tobin, M.J.; Vogel, C.; Whelan, D.R.; Wood, B.R.; Kwiatek, W.M. SR-FT-IR coupled with principal component analysis shows evidence for the cellular bystander effect. *Radiat. Res.* **2015**, *184*, 73–82. [CrossRef]

34. Pelton, J.T.; McLean, L.R. Spectroscopic Methods for Analysis of Protein Secondary Structure. *Anal. Biochem.* **2000**, *277*, 167–176. [CrossRef] [PubMed]

35. Barth, A. Infrared spectroscopy of proteins. *Biochim. Biophys. Acta* **2007**, *1767*, 1073–1101. [CrossRef] [PubMed]

36. Coe, J.V.; Nystrom, S.V.; Chen, Z.; Li, R.; Verreault, D.; Hitchcock, C.L.; Allen, H.C. Extracting Infrared Spectra of Protein Secondary Structures Using a Library of Protein Spectra, and the Ramachandran Plot. *J. Phys. Chem. B* **2015**, *119*, 13079–13092. [CrossRef] [PubMed]

37. Mei, Y.; Miller, L.; Gao, W.; Gross, R.A. Imaging the distribution and secondary structure of immobilized enzymes using infrared microspectroscopy. *Biomacromolecules* **2003**, *4*, 70–74. [CrossRef]

38. Delfino, I.; Portaccio, M.; Della Ventura, B.; Mita, D.G.; Lepore, M. Enzyme distribution and secondary structure of sol-gel immobilized glucose oxidase by micro-attenuated total reflection FT-IR spectroscopy. *Mater. Sci. Eng. C* **2013**, *33*, 304–310. [CrossRef]

39. Cai, S.; Singh, B.R. Identification of β-turn and random coil amide III infrared bands for secondary structure estimation of proteins. *Biophys. Chem.* **1999**, *80*, 7–20. [CrossRef]

40. Gault, N.; Rigaud, O.; Poncy, J.L.; Lefaix, J.L. Biochemical alterations in human cells irradiated with alpha particles delivered by macro- or microbeams. *Radiat. Res.* **2007**, *167*, 551–562. [CrossRef]

41. Li, J.Y.; Ying, G.G.; Jones, K.C.; Martin, F.L. Real-world carbon nanoparticle exposures induce brain and gonadal alterations in zebrafish (Danio rerio) as determined by biospectroscopy techniques. *Analyst* **2015**, *140*, 2687–2695. [CrossRef]

42. Dovbeshko, G.; Gridina, N.Y.; Kruglova, E.B.; Pashchuk, O.P. FT-IR Spectroscopy studies of nucleic acid damage. *Talanta* **2000**, *53*, 233–246. [CrossRef]

43. Lasalvia, M.; Perna, G.; Pisciotta, P.; Cammarata, F.P.; Manti, L.; Capozzi, V. Raman spectroscopy for the evaluation of the radiobiological sensitivity of normal human breast cells at different time points after irradiation by a clinical proton beam. *Analyst* **2019**, *144*, 2097–2108. [CrossRef] [PubMed]

44. Ricciardi, V.; Portaccio, M.; Piccolella, S.; Manti, L.; Pacifico, S.; Lepore, M. Study of SH-SY5Y cancer cell response to treatment with polyphenol extracts using FT-IR spectroscopy. *Biosensors* **2017**, *7*, 57. [CrossRef] [PubMed]

45. Yoshida, S.; Koike, K. Lipid and Membrane Dynamics in Biological Tissues—Infrared Spectroscopic Studies. *Adv. Planar Lipid Bilayers Liposomes* **2011**, *13*, 1–32.

46. Sailer, K.; Viaggi, S.; Nusse, M. Radiation–induced structural modifications in dsDNA analysed by FT–Raman spectroscopy. *Int. J. Radiat. Biol.* **1996**, *69*, 601–613. [CrossRef]

47. Barraza-Garza, G.; Castillo-Michel, H.; de la Rosa, L.A.; Martinez-Martinez, A.; Pérez-León, J.A.; Cotte, M.; Alvarez-Parrilla, E. Infrared spectroscopy as a tool to study the antioxidant activity of polyphenolic compounds in isolated rat enterocytes. *Oxidative Med. Cell. Longev.* **2016**, *2016*, 9245150. [CrossRef]

48. Kuhar, N.; Sil, S.; Verma, T.; Umapathy, S. Challenges in application of Raman spectroscopy to biology and materials. *RSC Adv.* **2018**, *8*, 25888–25908. [CrossRef]

49. Kumar, S.; Verma, T.; Mukherjee, R.; Ariese, F.; Somasundaram, K.; Umapathy, S. Raman and infra-red microspectroscopy: Towards quantitative evaluation for clinical research by ratiometric analysis. *Chem. Soc. Rev.* **2016**, *45*, 1879–1900. [CrossRef]

50. Gautam, R.; Chandrasekar, B.; Deobagkar-Lele, M.; Rakshit, S.; Umapathy, S.; Nandi, D. Identification of early biomarkers during acetaminophen-induced hepatotoxicity by Fourier transform infrared microspectroscopy. *PLoS ONE* **2012**, *7*, e45521. [CrossRef]

51. Zelig, U.; Kapelushnik, J.; Moreh, R.; Mordechai, S.; Nathan, I. Diagnosis of cell death by means of Infrared Spectroscopy. *Biophys. J.* **2009**, *97*, 2107–2114. [CrossRef]

52. Singh, J.K.; Dasgupta, A.; Adayen, T.; Shahmehdi, S.A.; Hammond, D.; Banerjee, P. Apoptosis is associated with an increase in saturated fatty acid containing phospholipids in the neuronal cell line, HN2–5. *Biochim. Biophys. Acta* **1996**, *1304*, 171–178. [CrossRef]

53. Delfino, I.; Perna, G.; Ricciardi, V.; Lasalvia, M.; Manti, L.; Capozzi, V.; Lepore, M. X-ray irradiation effects on nuclear and membrane regions of single SH-SY5Y human neuroblastoma cells investigated by Raman micro-spectroscopy. *J. Of Pharm. Biomed. Anal.* **2019**, *164*, 557–573. [CrossRef] [PubMed]

54. Vileno, B.; Jeney, S.; Sienkiewicz, A.; Marcoux, P.R.; Miller, L.M.; Forró, L. Evidence of lipid peroxidation and protein phosphorylation in cells upon oxidative stress photo-generated by fullerols. *Biophys. Chem.* **2010**, *152*, 164–169. [CrossRef] [PubMed]